

Transition to chaos in an acoustically driven cavity flow

Gaby Launay,^{1,*} Tristan Cambonie,^{1,†} Daniel Henry,^{1,‡} Alban Pothérat,^{2,§} and Valéry Botton^{1,3,||}

¹*Laboratoire de Mécanique des Fluides et d'Acoustique, CNRS, Université de Lyon, Ecole Centrale de Lyon, Université Lyon 1, INSA Lyon, ECL, 36 Avenue Guy de Collongue, 69134 Ecully CEDEX, France*

²*Coventry University, Priory Street, Coventry, United Kingdom*

³*INSA Euro-Méditerranée, Université Euro-Méditerranéenne de Fès, Route de Meknès, BP51, Fez, Morocco*



(Received 18 June 2018; published 8 April 2019)

We consider the unsteady regimes of an acoustically driven jet that forces a recirculating flow through successive reflections on the walls of a square cavity. The specific questions addressed are whether the system can sustain states of low-dimensional chaos when the acoustic intensity driving the jet is increased, and, if so, what are the pathway to it and the underlying physical mechanisms. We adopt two complementary approaches, both based on data extracted from numerical simulations: (i) We first characterize successive bifurcations through the analysis of leading frequencies. Two successive phases in the evolution of the system are singled out in this way, both leading to potentially chaotic states. The two phases are separated by a drastic simplification of the dynamics that immediately follows the emergence of intermittency. The second phase also features a second intermediate state where the dynamics is simplified due to frequency locking. (ii) Nonlinear time series analysis enables us to reconstruct the attractor of the underlying dynamical system and to calculate its correlation dimension and leading Lyapunov exponent. Both these quantities bring confirmation that the state preceding the dynamic simplification that initiates the second phase is chaotic. Poincaré maps further reveal that this chaotic state in fact results from a dynamic instability of the system between two nonchaotic states respectively observed at slightly lower and slightly higher acoustic forcing.

DOI: [10.1103/PhysRevFluids.4.044401](https://doi.org/10.1103/PhysRevFluids.4.044401)

I. INTRODUCTION

This paper deals with the wider issue of the pathway to chaos and turbulence in acoustically driven jet flows. Although the possibility of driving fluid motion by means of sound waves has been known since Michael Faraday [1], the systematic study of these flows has only recently been tackled [2,3]. While the basic mechanisms driving steady laminar flows are now well understood [4–7], the question of their stability remains a fundamental topic with more questions than answers [8–12]. Indeed, while the transition to turbulence in jets is a classical problem in fluid mechanics [13,14], acoustically driven jets have only recently aroused interest as a potential way of driving turbulence in fluids without the need for a direct mechanical contact. Such technologies are crucial for the manufacture of either delicate or aggressive materials that do not tolerate direct contact with the moving elements of a mechanical stirrer [15]. A typical example is the growth of crystals from

*gaby.launay@tutanota.com; [gabylaunay.github.io](https://github.com/gabylaunay)

†tristan.cambonie@gmail.com

‡daniel.henry@ec-lyon.fr; lmfa.ec-lyon.fr/spip.php?article368

§alban.potherat@coventry.ac.uk; users.complexity-coventry.org/~potherrat/index.html

||valery.botton@insa-lyon.fr; lmfa.ec-lyon.fr/spip.php?article271

a melt that is highly sensitive to impurities and more generally the stirring of a liquid during its solidification [8,16–21]. Though magnetic fields offer efficient solutions for contactless stirring, they demand high electric conductivities of the medium and can only act within a short distance of the walls of the fluid vessel. By contrast, ultrasonic waves emitted with a suitable frequency penetrate deep into the fluid and act regardless of the electric conductivity of the fluid. Nevertheless, the technological value of acoustic stirring would reside mostly in its ability to generate efficient mixing [22–24]. Since little is known of the chaotic or turbulent nature of these flows, the possibility of acoustically stirring flows in an effective way remains to be explored.

In typical configurations, an acoustic transducer is either directly inserted in the wall of a fluid vessel or placed in such a way as to generate an ultrasonic beam emitted from the wall into the fluid. The beam propagates along a straight centerline within the vessel where fluid is accelerated, creating a jet along the beam. Reflections may take place at the vessel walls, where two additional jets are generated: One alongside the walls and a second one driven by the reflected beam [7]. The stability properties of such a flow are to this day poorly known. Yet, fluctuations and oscillations observed in jets forced with sufficient acoustic power suggest that a form of transition to chaos or turbulence may potentially take place [3,12,25,26]. However, the nature of the transition and its underlying mechanisms remain to be found. In particular, it is not clear whether the system sustains states of low-dimensional chaos in further stages of development of this instability or how much acoustic forcing is required to reach a fully turbulent state.

In an attempt to answer the first of these two questions, we consider the generic geometry of a jet driven by acoustic streaming in a square cavity. The main jet is oriented at an angle with the walls so as to create a circulating flow pattern through successive reflections. We numerically simulate the flow to obtain the three-dimensional, time-dependent velocity and pressure fields and tackle the question of the transition to chaos in two ways. First, since the system sustains well-defined oscillations, it naturally lends itself to a frequency analysis, from which the emergence of chaos can be characterised by comparison to one of the classical scenarios (see Ref. [27] for a review of these scenarios). This method has been successful in showing that two-dimensional flows forced in a cavity, which bear resemblance with the confined flow we are considering, followed the Ruelle-Takens-Newhouse scenario [28]. The second approach involves dynamical systems analysis based on a time series extracted from the velocity field at different locations in the flow. This method offers a general way of characterizing complex dynamical systems (see Ref. [29] for a review), especially low-dimensional ones. Reconstructing the attractor of the system makes it possible to evaluate its chaotic nature. This is done by calculating the Lyapunov exponents that characterize how quickly two initially close states of the system may diverge during their evolution through the dynamics. The complexity of the system is further characterized by the correlation dimension of the attractor.

We first present the numerical simulations and analyze the flow regimes that are observed from a phenomenological point of view (Sec. II). Section III is dedicated to the characterization of the flow regimes by means of frequency analysis. Dynamical system properties are derived in Sec. IV.

II. FLOW SIMULATIONS

A. Studied configuration

We study the flow created by acoustic streaming in a cavity. The cavity is the same as in the experimental investigation by Cambonie *et al.* [26]: a closed rectangular vessel of square horizontal section that is filled with water (see Fig. 1). An acoustic beam, emitted by a 2-MHz circular plane transducer of diameter 28.5 mm, enters this cavity at the center of one of its vertical sides with an angle of $\pi/4$. As the acoustic near-field region is marbled by complex diffraction patterns and not essential to the core dynamics of the problem, it was physically separated from the investigation area to avoid unnecessary complexity. The distance between the transducer and the cavity is then adjusted so that the acoustic beam reaches the cavity close to its far-field region [6]. The acoustic beam reflects successively on the three other vertical walls before leaving the cavity through the

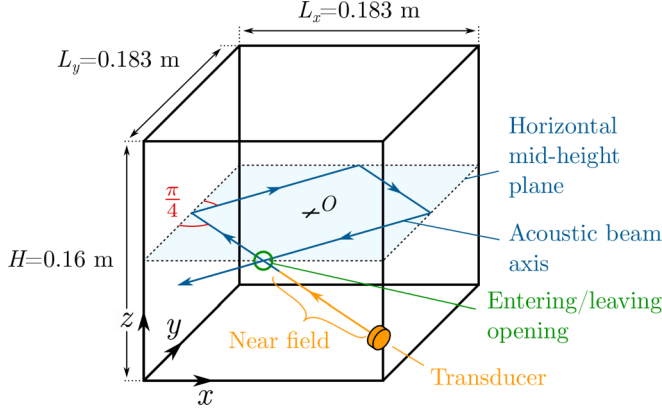


FIG. 1. Schematic representation of the cavity including the axis of the acoustic beam used to generate a circulating flow pattern. The acoustic beam enters the cavity by an opening in the center of one of its faces with an angle of $\pi/4$ and reflects on three of the vertical walls before leaving the cavity through the opening where it entered. The acoustic beam axis remains in the horizontal midheight plane (x, y) and is composed of four rectilinear parts. O is the origin of the reference frame used thereafter. This corresponds to the experimental setup used by Cambonie *et al.* [26]. The plane transducer is 28.5 mm in diameter and operates at 2 MHz.

opening where it entered. The resulting beam path is a broken line forming a square at half-height of the cavity (see Fig. 1). For the sake of simplicity, we will refer to the plane containing the acoustic beam axis as the horizontal midheight plane. The flow is driven by an acoustic streaming forcing in the volume inside this beam, and forms a practically square pattern inside the cavity [26].

B. Physical model

The flow in such a configuration is governed by the Navier-Stokes equations with a force term corresponding to the acoustic forcing. As indicated by Moudjed *et al.* [7], this force term can be written as

$$\mathbf{F}(x, y, z) = \frac{2\alpha I_{ac}(x, y, z)}{c} \mathbf{e}_p, \quad (1)$$

where \mathbf{F} is the force per unit of volume ($\text{kg m}^{-2} \text{s}^{-2}$), α is the acoustic attenuation (m^{-1}), I_{ac} is the acoustic intensity (W m^{-2}), c is the sound velocity (m s^{-1}), and \mathbf{e}_p is the acoustic beam direction of propagation. I_{ac} can be further expressed as $I_{ac} = I_0 I(x, y, z)$, with I_0 being the acoustic intensity amplitude (W m^{-2}) and $I(x, y, z)$ being the normalized acoustic intensity distribution. According to Blackstock [30], the acoustic intensity amplitude I_0 is directly related to the transducer acoustic power P_{ac} (W) by $I_0 = P_{ac}/(\pi R_t^2/4)$, where R_t is the transducer radius (m). The acoustic force can then be written as

$$\mathbf{F}(x, y, z) = \left[\frac{2\alpha P_{ac}}{c\pi R_t^2} \right] 4I(x, y, z) \mathbf{e}_p. \quad (2)$$

The problem is made dimensionless using the cavity height H as length scale, ν/H as velocity scale, H^2/ν as timescale, and $\rho\nu^2/H^2$ as pressure scale, with ρ being the fluid density and ν being the kinematic viscosity. The dimensionless equations to solve in the cavity are then

$$\nabla \cdot \mathbf{u} = 0, \quad (3)$$

$$\frac{\partial \mathbf{u}}{\partial t} + (\mathbf{u} \cdot \nabla) \mathbf{u} = -\nabla p + \nabla^2 \mathbf{u} + A^* 4I(x, y, z) \mathbf{e}_p, \quad (4)$$

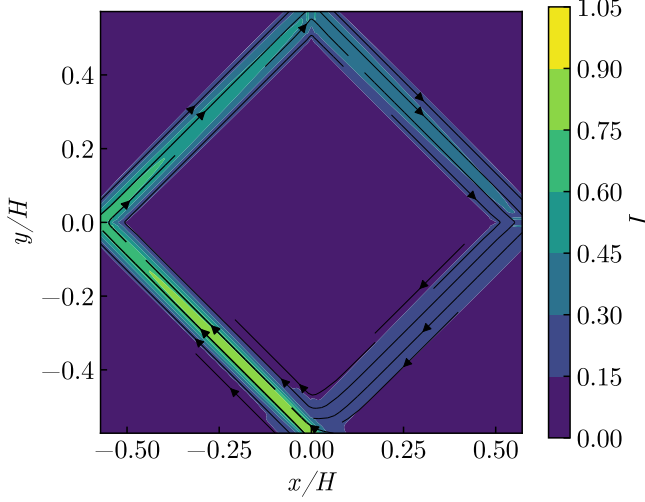


FIG. 2. Normalized acoustic forcing I generated by the acoustic beam in the horizontal midheight plane ($z/H = 0$), computed using the Rayleigh integral. The acoustic beam enters at $(x/H = 0, y/H = -0.571875)$, the center of a vertical wall, with a $\pi/4$ angle and is reflected on the other vertical walls while slowly diverging and dissipating (which explains the progressive loss of intensity), before leaving the cavity at its inlet location.

with A^* , the dimensionless magnitude of the acoustic forcing, given by

$$A^* = \frac{2\alpha P_{ac} H^3}{c\pi R_t^2 \rho v^2}. \quad (5)$$

Instead of A^* , we shall use the quantity $A = 10^{-6}A^*$ as the sole control parameter. With this choice, $A = 1$ corresponds to a dimensional power P_{ac} of 1 W, for the parameters of Ref. [26]'s experiment (i.e., $\alpha = 0.1 \text{ m}^{-1}$ for a 2-MHz transducer, $\rho = 10^3 \text{ Kg m}^{-3}$, $c = 1480 \text{ m s}^{-1}$, $v = 9.3 \cdot 10^{-7} \text{ m}^2/\text{s}$, $R_t = 0.01425 \text{ m}$, and $H = 0.16 \text{ m}$).

The normalized acoustic intensity distribution $I(x, y, z)$ in the cavity is computed for the above parameters by means of the Rayleigh integral for each beam [7,30]. These beams come from virtual sources obtained as images of the acoustic source through successive symmetries with respect to the different walls where the reflections occur. The progressive attenuation of the acoustic beam along its propagation path is taken into account. More details on diffraction, attenuation, and reflection at the walls can be found in Ref. [7]. In particular, these authors have shown that the treatment of the zones where incident and reflected beams interfere is not crucial to reliably derive the flow pattern. For each reflection zone, we have then chosen to use the incident field up to the vertical normal plane and the reflected beam beyond this plane. These results are presented in Fig. 2. Note that, because of the divergence and dissipation of the acoustic beam, the four branches of the forcing are not identical. Consequently, the only symmetry of the forcing is about the $z = 0$ plane.

C. Numerical simulations

The simulations of the flow driven by this steady acoustic forcing are run using a spectral finite-element method [31], with a grid comprising two elements in the vertical direction (along z , with 21 points per element) and two elements in each of the two horizontal directions (with 31 points per element). In each element, the spatial discretization is obtained through Gauss-Lobatto-Legendre point distributions which are naturally tightened along the element boundaries. The time discretization is carried out using a semi-implicit splitting scheme, as proposed by Karniadakis *et al.* [32]: The nonlinear terms are first integrated explicitly, the pressure is then solved through a pressure

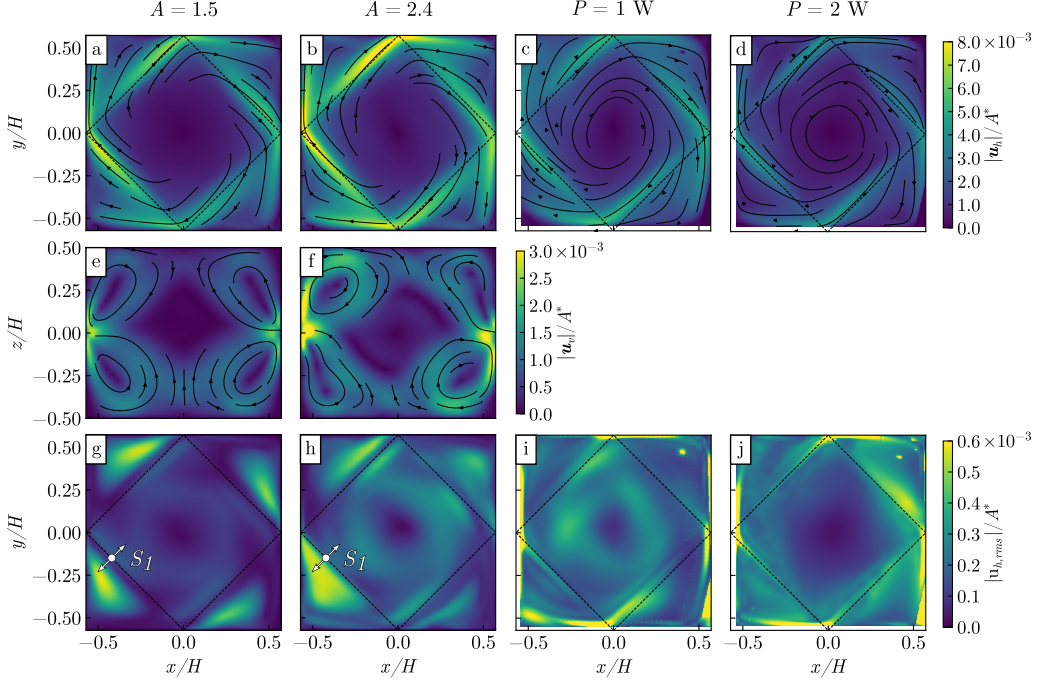


FIG. 3. Normalized time-averaged velocity fields and rms fluctuations for various acoustic forcing. [(a), (d)] In-plane velocity magnitude $|\bar{\mathbf{u}}_h|/A^*$ and segments of 2D streamlines in the horizontal midheight plane ($z/H = 0$). [(a), (b)] Numerical results for $A = 1.5$ and $A = 2.4$. Dashed lines represent the acoustic beam axis. [(c), (d)] Experimental Particle Image Velocimetry (PIV) measurements for $P = 1$ W and $P = 2$ W. The velocity fields are normalized using respectively $A^* = 1.5 \times 10^6$ and $A^* = 2.4 \times 10^6$ for the sake of the comparison with the numerical results. Dashed lines represent the expected position of the acoustic beam. [(e), (f)] In-plane velocity magnitude $|\bar{\mathbf{u}}_v|/A^*$ and segments of 2D streamlines in the vertical plane ($y = 0$) for $A = 1.5$ and $A = 2.4$. [(g), (h)] Normalized rms fluctuations $|\mathbf{u}_{h,rms}|/A^*$ in the horizontal midheight plane for $A = 1.5$ and $A = 2.4$. S_1 is the point where velocity time series are recorded for subsequent spectral and nonlinear dynamics analyses. Arrows on this point indicate the transverse direction. [(i), (j)] Normalized experimental rms fluctuations $|\mathbf{u}_{h,rms}|/A^*$ in the horizontal midheight plane for $P = 1$ W and $P = 2$ W.

equation enforcing the incompressibility constraint (with a consistent pressure boundary condition derived from the equations of motion), and the linear terms are finally integrated implicitly. This time integration scheme is used throughout our numerical simulations with the third-order accurate formulation described in Karniadakis *et al.* [32]. A no-slip boundary condition is applied at all the cavity walls.

In our configuration, the acoustic forcing principally occurs in the neighborhood of the horizontal midplane. In order to accurately take into account this forcing, which is imposed at the grid points, we use a multielement spectral approach allowing us to choose two elements in the vertical direction. The mesh is then refined at midheight with 13 discretization points on the width of the acoustic intensity peak and jet velocity peak. Tests with different meshes have ensured that this choice provides a good discretization of the imposed acoustic forcing and a good precision for the calculation of the main flow which also occurs in this region at midheight of the cavity. Figure 3 presents a comparison of the experimental and numerical time-averaged and rms velocity fields in the horizontal midheight plane. In the experimental case, the relation between the acoustic power (P) and the acoustic forcing (A) is not known, making *a priori* comparison difficult. Instead, cases that, as best as possible with the available data, exhibit the same typical values of velocity

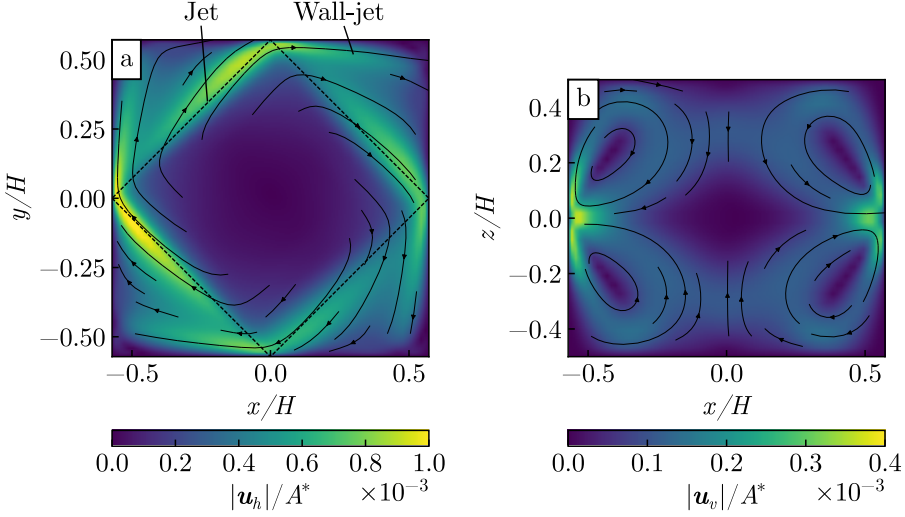


FIG. 4. Normalized velocity fields for a steady configuration ($A = 1$). (a) In-plane velocity magnitude $|\mathbf{u}_h|/A^*$ and segments of 2D streamlines in the horizontal midheight plane ($z = 0$). Dashed lines represent the acoustic beam axis. (b) In-plane velocity magnitude $|\mathbf{u}_v|/A^*$ and segments of 2D streamlines in the vertical plane ($y = 0$).

a posteriori are presented. The numerical simulations reproduce well the time-averaged topology of the experimental flow [Figs. 3(a)–3(d)], featuring the four successive jets and their associated wall jets. Regarding the rms of the velocity [Figs. 3(g)–3(j)], the flow behaviors are qualitatively similar, albeit with more localized peaks of intensity in the zones where the beam reflects on the wall in the experiments. Nevertheless, in the absence of sufficient control of the acoustic force in the experiment, it is difficult to push the comparison further than the qualitative level.

D. Flow overview

To investigate this flow, we first present its global evolution with the acoustic forcing A (mean flow and fluctuation distribution). We then deepen our analysis by considering the velocity time series at specific locations and for different values of A .

For low values of the acoustic forcing ($A < 1.5$), the system is steady. An example of steady state flow is presented in Fig. 4 for $A = 1$ through the values of the velocity norm at midheight and in the $y = 0$ vertical plane. For moderately low acoustic forcing ($A > 0.5$, see Ref. [26]), a jet reaching a wall generates (i) a wall jet by inertial effect, which remains in the vicinity of the wall [see Fig. 4(a)], and (ii) vertical velocities, which create recirculation zones above and below the horizontal midheight plane [see Fig. 4(b)]. This flow features two quasisymmetries, a four-quadrant quasisymmetry around the z axis [visible in Fig. 4(a)], and a symmetry with respect to the horizontal midheight plane [up-down symmetry visible in Fig. 4(b)].

For $A = 1.5$, the system becomes periodic, with velocity fluctuations concentrated between the impinging jets and the walls [see Fig. 3(g)]. The dimensionless period associated to this oscillation $T = 7.03 \times 10^{-3}$ is of the same order as the period measured by Cambonie *et al.* [26] ($T = 6.40 \times 10^{-3}$ for $A \approx 1$). Oscillations featured in this configuration are strongly three dimensional (3D) and complex in structure. This makes it challenging to identify the instability generating them. However, the topology of the time-averaged velocity field [in both horizontal and vertical planes, respectively, in Figs. 3(a) and 3(e)] remains very similar to that for $A = 1$, and the distribution of the rms velocity fluctuations shares the four-quadrant quasisymmetry of the time-averaged flow [see Fig. 3(g)].

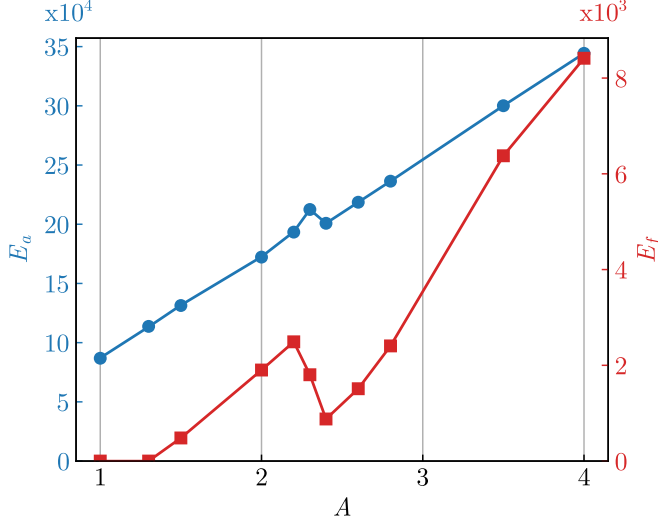


FIG. 5. Evolution of the cavity flow energy with increasing acoustic forcing A . Blue circles: time-averaged energy E_a in the cavity, from Eq. (6). Red squares: fluctuation energy E_f in the cavity, from Eq. (7).

For acoustic forcing between $A = 1.5$ and $A = 2.2$, the time-averaged flow topology remains very similar (not shown here). In particular, it conserves the up-down and four-quadrant quasisymmetries. However, the energy of both the time-averaged flow and the fluctuations increases, as shown in Fig. 5, as a result of the higher forcing. The energy values presented in this figure are obtained by computing the integral of the dimensionless kinetic energy over the cavity volume V :

$$E_a = \frac{1}{2} \int_V |\bar{\mathbf{u}}|^2 dV, \quad (6)$$

$$E_f = \frac{1}{2} \int_V u_{\text{rms}}^2 dV. \quad (7)$$

The time-averaged and rms velocity fields are defined as

$$\bar{\mathbf{u}} = \frac{1}{t_f} \int_{t=0}^{t=t_f} \mathbf{u} dt, \quad (8)$$

$$u_{\text{rms}} = \left[\frac{1}{t_f} \int_{t=0}^{t=t_f} |\mathbf{u} - \bar{\mathbf{u}}|^2 dt \right]^{\frac{1}{2}}, \quad (9)$$

with t_f being the duration of the simulation.

For $A = 2.4$, both vertical and horizontal symmetries are broken: While the time-averaged flow in the horizontal midheight plane [Fig. 3(b)] remains similar to that for $A = 1.5$, the time-averaged flow in the vertical plane [Fig. 3(f)] and the fluctuations in the horizontal midheight plane [Fig. 3(h)] lose symmetry. This reflects a major change in the flow dynamics, which is confirmed by the sudden decrease in the fluctuation energy E_f for $A = 2.4$ (Fig. 5).

For an acoustic forcing in the range $A = 2.4$ to $A = 4$, the time-averaged and fluctuation energies keep increasing (see Fig. 5), but neither the topology of the average flow nor that of the velocity fluctuations evolve significantly. It is noteworthy that Cambonie *et al.* [26] observed more significant alterations of the time-averaged flow topology in the midheight horizontal plane for a wider range of acoustic forcing ($A \in [0.5, 8]$).

The configuration for $A = 2.3$ appears to be transitional in terms of energy evolution (see Fig. 5), but still exhibits the vertical and horizontal symmetries seen at lower acoustic forcing. In contrast

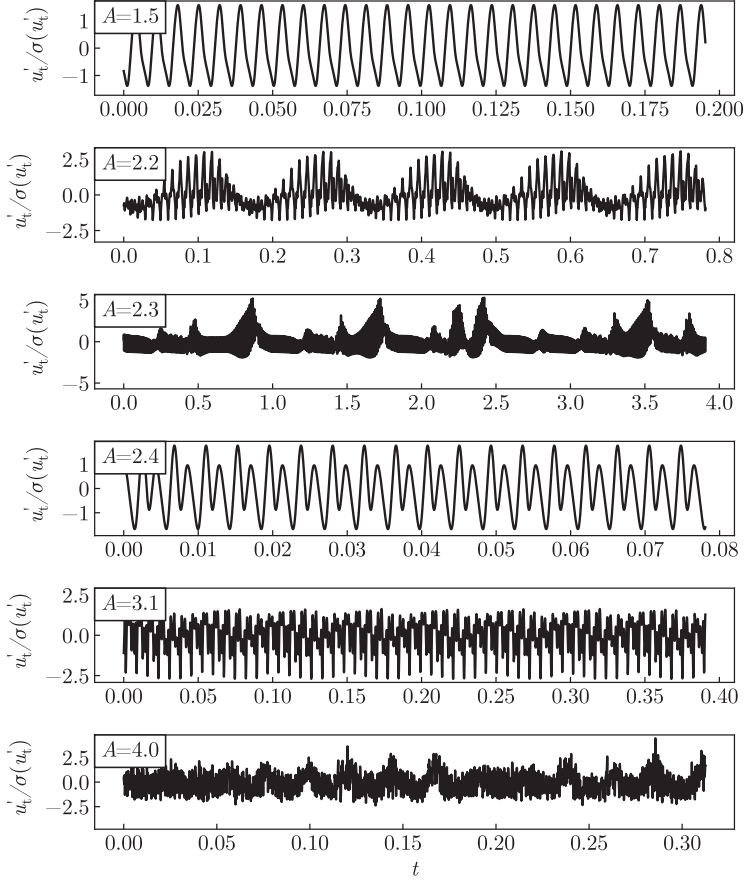


FIG. 6. Temporal evolution of the jet transverse velocity fluctuation (u'_t) for increasing acoustic forcing A . The transverse velocity fluctuation u'_t is the fluctuating part of the velocity component perpendicular to the acoustic axis, in the horizontal midheight plane at point S_1 [see point S_1 and associated arrows in Figs. 3(g) and 3(h)]. The velocity is normalized by the standard deviation of the velocity fluctuations $\sigma(u'_t)$. Note that the durations observed on these plots correspond to several hours in physical time (5×10^3 to 10^5 s). It is worth stressing that such long time series are indispensable to adequately represent the system's dynamics. However, experimentally obtaining data over such long periods of time would be extremely difficult.

to the relatively gentle changes in the mean and fluctuation fields within the ranges $A = 1.5$ to $A = 2.3$ and $A = 2.4$ to $A = 4$, the time series of the jet velocity is significantly altered within these same ranges (see Fig. 6). More specifically, (i) the fluctuations change from almost sinusoidal to quasiperiodic between $A = 1.5$ and $A = 2.2$. (ii) For $A = 2.3$, the velocity fluctuations are rather complex, with no apparent periodicity. (iii) At $A = 2.4$, the time series again adopts a periodic behavior. (iv) Between $A = 2.4$ and $A = 4.0$, the series progressively loses any apparent periodicity or structure.

The nontrivial succession of periodic, quasiperiodic, periodic again, and eventually seemingly random regimes is reminiscent of classical transition scenarios to chaos. It occurs over a range of parameters that is consistent with the experimental observations of Cambonie *et al.* [26].

III. SCENARIO FOR THE TRANSITION TO CHAOS

The sequence of flow regimes observed in the fluctuations (Fig. 3) and time series (Fig. 6) shows that overall the flow transits to more chaotic states as the forcing parameter A is increased.

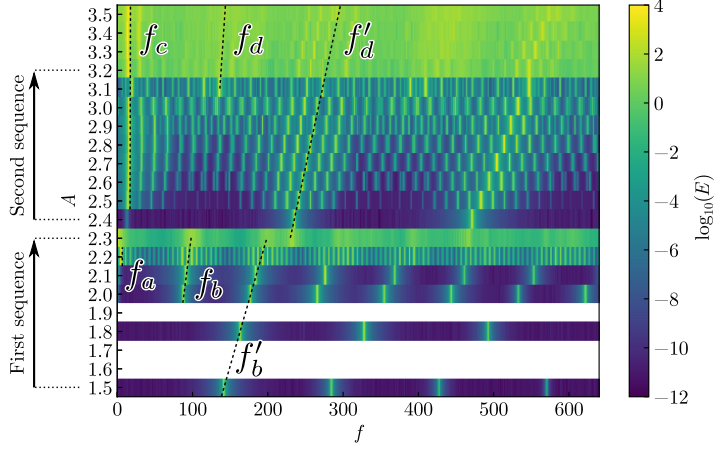


FIG. 7. Power spectral density E as a function of the acoustic forcing A and the frequency f . E is computed using fast Fourier transform of the time series of u'_t following Welch's method [39]. This picture singles out the appearance of frequencies associated with bifurcations (Hopf and period doubling) and highlights potentially chaotic regimes (at $A = 2.3$ and $A > 3.2$). Dashed lines identify particular frequencies evolving with A . Note that the observed range of frequency values is consistent with the very low frequencies experimentally observed by Cambonie *et al.* [26] (of the order of 5×10^{-3} Hz, or $f = 128$).

This evolution, however, presents unusual features, such as the brutal change in flow topology and fluctuation energy that occurs between $A = 2.2$ and $A = 2.4$ (see Fig. 5). Classically, the route to chaos follows one of the three canonical scenarios: (i) Successive appearance of low frequencies (Hopf bifurcations) are observed in the Ruelle-Takens-Newhouse scenario [33]. In this scenario, the chaotic behavior typically appears after three bifurcations [34]. (ii) Succession of period-doubling bifurcations are part of the Feigenbaum scenario [35–37]. In this scenario, chaos can appear after a very large number of bifurcations of this type. (iii) Appearance of intermittent chaotic events that occupy an increasingly large fraction of the timeline (intermittency phenomenon) are observed in the Pomeau-Manneville scenario [38]. The characteristic features of each of these scenarios can be tracked in the evolution of the dominating frequencies of the system, and through the possible occurrence of intermittent behavior (see, for example, Ref. [27]). Following this idea, we shall now analyze the main frequencies of velocity fluctuations and seek similarities with the classical scenarios for the transition to chaos. For this, we will focus on u'_t , the fluctuation of the horizontal velocity component transverse to the first beam axis at point S_1 [see Figs. 3(g) and 3(h)]. Figure 7 shows the power spectral density E for different values of the acoustic forcing A extracted from the time series of u'_t . It has been verified that the peak frequencies appearing in the power spectral densities are independent of the position in space within the cavity, as long as they are extracted from an area with significant fluctuation intensity.

A. Spectral signature of the different regimes

For the two lowest acoustic forcings ($A = 1.5$ and $A = 1.8$), the flow is periodic and the power spectral densities show a peak frequency (denoted f'_b in Fig. 7, at $f = 143$ and $f = 164$, respectively, for $A = 1.5$ and $A = 1.8$) along with harmonics at higher frequencies. These very low frequencies (on the order of 5×10^{-3} Hz) are consistent with the experimental observations by Cambonie *et al.* [26]. The peak frequency increases linearly with A and can be traced up to $A = 2.3$. From $A = 2.0$, a peak at half frequency $f_b = 0.5f'_b$ appears, indicating a period doubling. f_b also increases with A and exists up to $A = 2.3$. A series of successive period doublings is one of the three identified scenarios of transition to chaos [34]. In the present case, however, the next peak, which

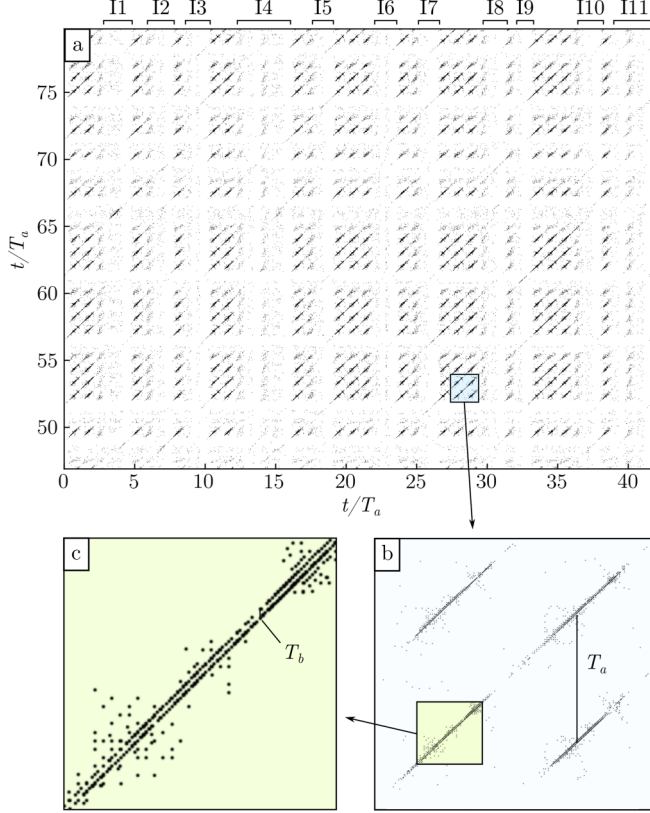


FIG. 8. (a) Recurrence map of u'_t for acoustic forcing $A = 2.3$. The regions with diagonal patterns correspond to time intervals for which the system is quasiperiodic. White horizontal and vertical bands correspond to intermittencies, for which the dynamical system's evolution loses quasiperiodicity. For the sake of simplicity, only a portion of the signal is represented here, where only 11 of the 25 intervals of intermittent behavior ($I1$ to $I11$) from the full measured signal are visible. [(b), (c)] Enlargements of the recurrence map. T_a and T_b are the periods associated with the characteristic frequencies f_a and f_b on Fig. 7.

appears for an acoustic forcing $A = 2.2$, is at a far lower frequency $f_a = 7$. f_a is not commensurate with f_b and results from a Hopf bifurcation (as defined by Eckmann [34]). The harmonics of this fundamental frequency are visible across the entire resolved spectrum. In particular, they interfere with the peak frequencies associated with f_b and f'_b .

The next dynamical change occurs at $A = 2.3$, where the energy suddenly spreads across the spectrum. This can be seen as the floor level of the spectrum raises from noise level (about 10^{-10}) at $A = 2.2$ to 10^{-3} at $A = 2.3$. This opens the door to a possible intermittent behavior, which is indeed detected by means of the recurrence map shown in Fig. 8. On this map, each black dot on a recurrence represents two moments in time (respectively on abscissa and ordinate) for which the system states are close in the phase space (here, two moments where u'_t values differ by less than 0.1% of the total velocity fluctuation amplitude). Consequently, diagonal lines formed by succession of dots represent time intervals for which the signal is correlated. Hence, periodic signals show up as diagonal lines distant by the signal period. For $A = 2.3$, a portion of the recurrence map computed in a phase space of dimension 3 is presented in Fig. 8(a). This map exhibits regions of quasiperiodicity (diagonal patterns), separated by horizontal and vertical white bands (marked as $I1$ to $I11$), for which the dynamical system exhibits a behavior where quasiperiodicity is lost. This is the signature of intermittencies. For comparison, a recurrence map that features no intermittencies ($A = 2.2$)

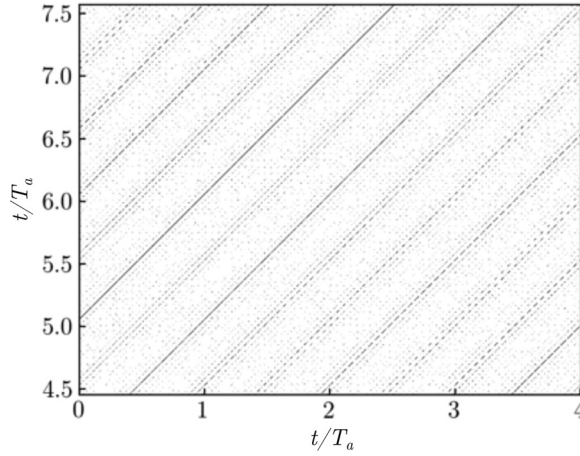


FIG. 9. Recurrence map of u'_t for an acoustic forcing $A = 2.2$. The diagonal patterns indicating a quasiperiodic behavior are clearly visible on this figure.

is shown in Fig. 9. Zooming on a region with diagonal patterns [Figs. 8(b) and 8(c)] reveals the frequencies of the quasiperiodic signal: $f_a = 1/T_a = 6.92$ and $f_b = 1/T_b = 113$, in agreement with the frequencies identified on the power spectral density (Fig. 7).

For $A = 2.4$, the power spectral densities reflect a drastic simplification of the dynamics, which reverts to being periodic. This simplification coincides with the drop of fluctuation energy observed in Fig. 5. The fundamental frequency at $A = 2.4$ reads $f'_d = 236$, increases linearly with A , and exists up to $A = 3.5$. At $A = 2.5$, a Hopf bifurcation gives birth to a low frequency $f_c = 15.9$, similar to what occurs at $A = 2.2$. At $A = 3.1$, a period-doubling bifurcation produces a frequency $f_d = f'_d/2 = 137$, as well as a substantial shift of the frequency f_c toward a higher value. Finally, for $A \geq 3.2$ (including $A = 4$, not shown here), the energy spreads across the spectrum, as expected for chaotic systems. Nevertheless, the peak frequencies exhibited at $A = 3.1$ can still be traced in the continuous spectra.

B. Evolution of the frequencies with the forcing parameter A and frequency locking

The evolution of the frequencies identified above gives a first indication on the underlying flow dynamics. We have noted that the high frequencies (namely f_b , f_d , and their harmonics) evolve linearly with the acoustic forcing A (see Fig. 7). The low-frequency f_c , in contrast, does not evolve monotonically (Fig. 10). All of these variations, however, remain smooth, with the notable exception of configurations with acoustic forcing between $A = 3.1$ and $A = 3.13$, where f_c suddenly shifts to a higher frequency and f_d also undergoes little discontinuities.

These first discontinuities may be understood by recalling that when two oscillating phenomena coexist in a single dynamical system, the spectra exhibit frequency peaks at their linear combinations (explaining the numerous peaks observed at $A = 2.2$ and in the range $A \in [2.5, 3.1]$ in Fig. 7). However, if the ratio between these two frequencies happens to be a rational number, the dynamics can be drastically simplified. This effect is called *frequency locking* [27]. For these specific values, one can expect much simpler dynamics, compared to neighboring values of A . This is, for example, the case for configurations with acoustic forcing between $A = 3.1$ and $A = 3.13$, where $f_d/f_c = T_c/T_d = 13/2$, meaning that the oscillation periods associated to f_c and f_d are in a ratio of 13 to 2. This simplification is clearly visible on the evolution of the dimension of the system, which will be presented in Sec. IV B. The existence of frequency locking on an interval of the governing parameter is known in nonlinear dynamical system theory as “Arnold’s tongue” [27].

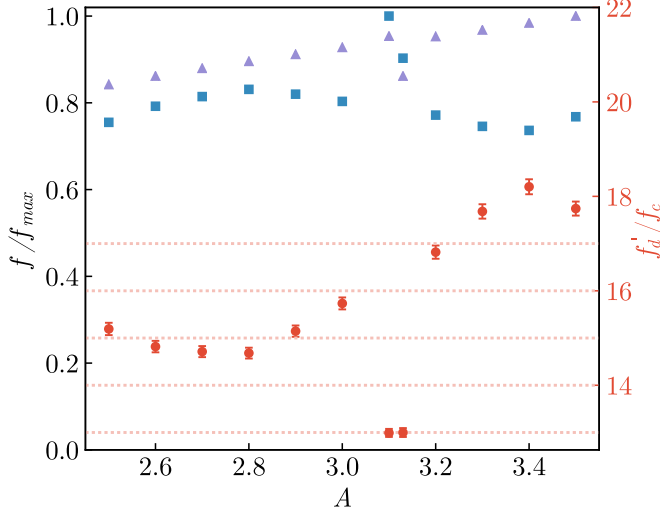


FIG. 10. Evolution of characteristic frequencies with the acoustic forcing A . Blue squares: normalized frequency f_c . Purple triangles: normalized frequency f'_d . Red circles: ratio f'_d/f_c (right axis). The peak frequencies are obtained from local maxima in the power spectral densities, and hence bear an uncertainty $\Delta f/f_{\max} = 1/(t_f f_{\max}) < 4.5 \times 10^{-4}$ linked to the time-series duration t_f . The frequency f_c appears to evolve smoothly, with the exception of the cases between $A = 3.1$ and $A = 3.13$, where it is abnormally high. The fact that the ratio f'_d/f_c is an integer for these cases suggests that this abnormal behavior is due to frequency locking.

The evolution of the main frequencies displays a second set of discontinuities when the dynamics suddenly simplify at $A = 2.4$: Although f'_d , f_d , and f_c are respectively close to f'_b , f_b , and f_a , their evolution exhibits a discontinuity in the range $A = 2.3$ to $A = 2.4$ (see Fig. 7). We shall analyze this phenomenon more in detail in Sec. IV D.

C. Scenario for the transition to chaos

The evolution of our system exhibits elements of all three canonical scenarios of transition to chaos (Ruelle-Takens-Newhouse, Feigenbaum, and Pomeau-Manneville) but complies fully with none of them. A potentially chaotic regime first appears for $A = 2.3$, where intermittency is observed. It follows a first Hopf bifurcation to the periodic basic state and then a period-doubling bifurcation and a Hopf bifurcation. After the dynamics has simplified back to a periodic state, another two bifurcations are needed for chaos to appear again. This time, the period doubling and the Hopf bifurcations appear in reverse order. The most striking difference with the three established scenarios of transition to chaos is the sudden simplification of the dynamics that occurs at $A = 2.4$, which implies that two distinct ranges of the forcing parameter can potentially lead to chaos. These two distinct ranges will be referred to as the first and second sequences in the sequel. This peculiar feature raises two questions: First, do both ranges of regimes where a continuous frequency spectrum is observed support actual chaos? And second, which mechanisms lead to the simplification observed at $A = 2.4$? We shall now attempt to answer these questions.

IV. CHARACTERIZATION OF THE DYNAMICAL SYSTEM

Chaotic dynamical systems cannot be fully characterized by means of frequency spectra. In particular, spectra do not offer a way to distinguish stochastic systems from chaotic but still deterministic ones, as both exhibit continuous spectra. To ascertain the possible chaotic nature of the

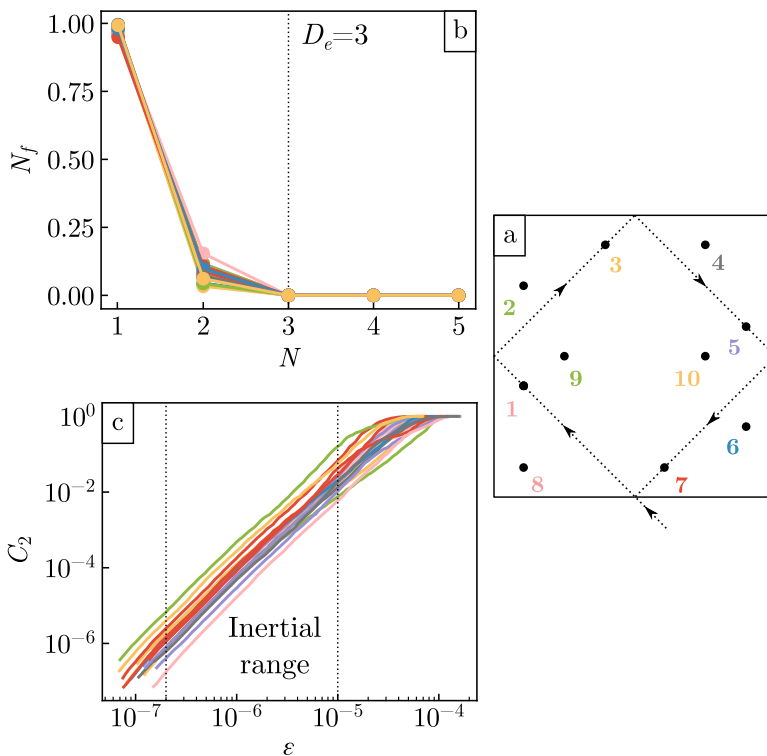


FIG. 11. False neighbors number N_f and correlation sums C_2 for $A = 2.3$ from velocity time series taken at different positions in the cavity. (a) Illustration of the positions investigated in the cavity midheight plane. The dashed line is the axis of the acoustic beam. (b) The fall to zero of the number of false neighbors indicates a global embedding dimension of $D_e = 3$. (c) The power law exponent of C_2 in the inertial range gives the correlation dimension D_2 . The spatial homogeneity of D_e and D_2 in this case suggests that the whole cavity is governed by the same dynamical system.

system, we shall now seek to characterize the underlying dynamical system by means of nonlinear time-series analyses. More specifically, we shall seek the conditions in which the dimension of the dynamical system becomes fractal and when sensitivity to initial conditions, as measured by Lyapunov exponents, betrays a chaotic behavior.

The nonlinear dynamics analysis is performed on time series of the velocity (generally u'_t , as used in Sec. III), denoted $s(t)$ from now on. As for the power spectral densities, we checked that all quantities derived in this section are location independent. As an example, the correlation sum (used to compute the correlation dimension D_2) is plotted for $A = 2.3$ and for several positions inside the cavity in Fig. 11. To ensure that the signals are long enough to capture the whole dynamics of the system, the nonlinear properties presented thereafter were computed for increasing signal length, until proper convergence was attained (i.e., less than 1% difference between the nonlinear properties computed on a given signal and on 75% of it).

A. Attractor

We start by visualizing the time-series dynamics in the phase space using the method of delays. The first step in achieving this is to find a timescale Δt^* that is sufficiently short to capture the fastest timescale of the system and, at the same time, sufficiently long for the system to actually evolve between time steps. As recommended by Kantz and Schreiber [40], we shall define Δt^* as

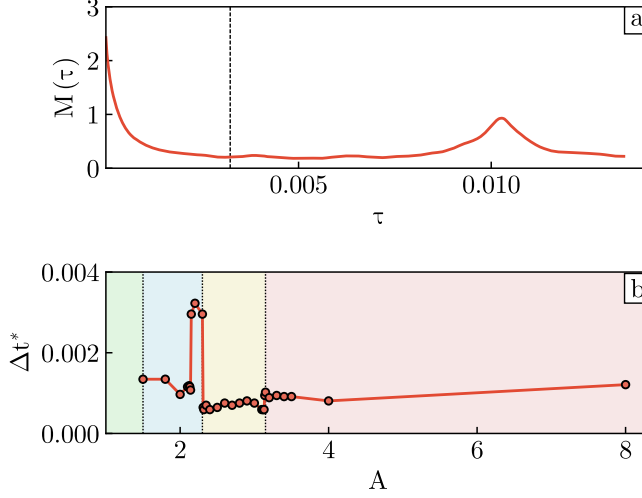


FIG. 12. (a) Example of mutual information computed from u'_t for $A = 2.2$. The first minimum is highlighted by the vertical dashed line and gives an optimal timescale $\Delta t^* \approx 0.003$. (b) Evolution of the optimal time scale Δt^* with the acoustic forcing A . From left to right, the vertical dotted lines delimit the regions identified on Fig. 7: the steady region (green), the first sequence (blue), the second sequence (orange), and the regimes with an attractor of higher dimensions (red).

the time interval that corresponds to the first minimum of the mutual information $M(\tau)$,

$$M(\tau) = \sum_{ij} p_{ij}(\tau) \ln \frac{p_{ij}(\tau)}{p_i p_j}, \quad (10)$$

where p_i is the probability to find the value of time series in the i th interval and $p_{ij}(\tau)$ is the joint probability that an observation falls into the i th interval and the observation after a time τ falls into the j th interval. Abarbanel *et al.* [29] point out that this method provides better results for systems with a nonlinear behavior than the alternative definition of Δt^* based on the first zero of the correlation function. Figure 12(a) shows a typical example of mutual information $M(\tau)$, while the variations of the optimal timescale Δt^* with A are shown in Fig. 12(b). The high value of Δt^* for $A \in [2.2, 2.3]$ is correlated to the appearance of low frequencies (see Fig. 7).

Knowing Δt^* , it is then possible to build a representation of the attractor in the three-dimensional phase space (chosen for obvious practical reasons, without prejudging of the actual dimension of the attractor), by defining the delay vector:

$$\mathbf{x}(t) = [s(t), s(t - \Delta t^*), s(t - 2\Delta t^*)]. \quad (11)$$

Figure 13 shows the evolution of the attractor as A varies. These representations of the attractors give a qualitative view of how the dynamics of the system evolves (as an example, a movie showing orbits spanning the attractor for $A = 2.2$ is provided in the Supplemental Material [41]). The succession of regimes observed in the physical space and on the power spectral densities in Sec. III can again be easily traced in this representation. In particular, the two sequences identified in Fig. 7 are clearly visible here. Both first start with an attractor of simple shape ($A = 1.5$ and $A = 2.4$). Attractors then evolve into more complex shapes that nevertheless retain a legible representation in three

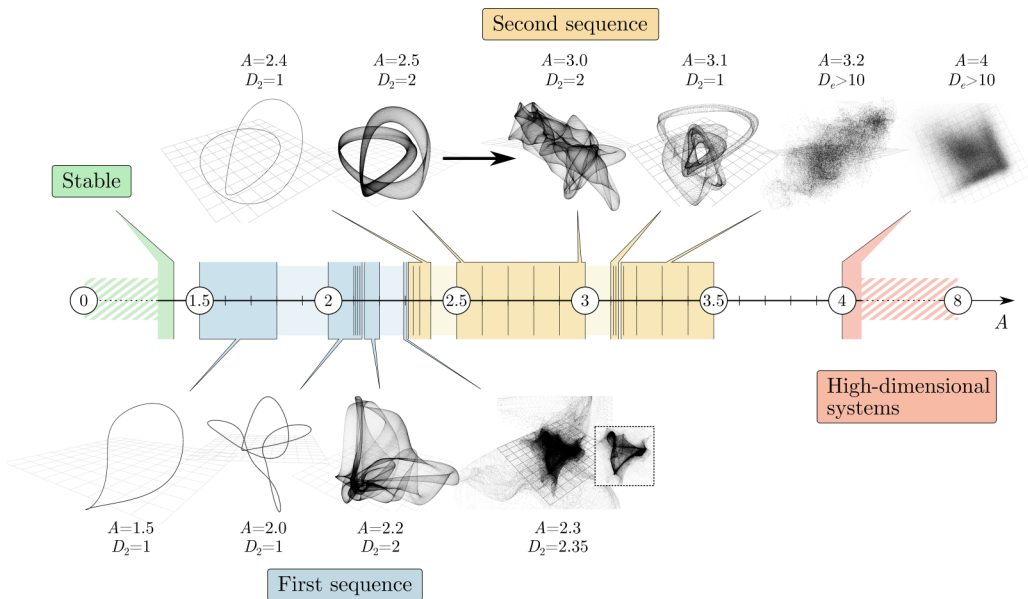


FIG. 13. Evolution of the attractors represented in three-dimensional phase spaces $[s(t), s(t - \Delta t^*), s(t - 2\Delta t^*)]$ for increasing acoustic forcing A . Each vertical bar represents an acoustic forcing for which nonlinear properties were computed from time series of the velocity. The first sequence (bottom attractors) and second sequence (top attractors) leading up to chaos are clearly visible. Gaps in this evolution represent regions where the dynamics fundamentally changes (as reflected by the dimensions of the attractors).

dimensions. In the last phase of both sequences, the attractors end up in a shape that tells little to the naked eye ($A = 2.3$ and $A = 4$).

B. Embedding and correlation dimensions

To reconstruct the system's attractor (not necessarily lying in a three-dimensional space), we need to find its dimension, which may be or may not be an integer. For this, we must first find its *embedding dimension* D_e , which is the dimension of the smallest linear space that contains it. D_e is found by the method of false neighbors [42], which relies on the observation that if an attractor is represented in a dimension $N < D_e$, then orbits may cross each other, and points of the attractor that would be far from each other in a space of dimension D_e would falsely appear as neighbors in a “folded” N -dimensional representation. In practice, false neighbors are defined as points of the phase space that are close but for which the subsequent trajectories differ. The embedding dimension D_e is then the lowest dimension N for which the number of false neighbors falls to zero. To estimate if two trajectories differ or not, a critical divergence ratio r is used. Finding an adequate value for this ratio r can be challenging, especially for chaotic attractors. Kennel *et al.* [42] recommend carrying out the false neighbors analysis for a divergence ratio in the range $[10, 40]$ to ensure significant confidence in the value of D_e . In this study, coherent values of D_e could only be found for $r \in [20, 30]$. To remove the uncertainty on the embedding dimension D_e , we performed an additional inspection of the Poincaré sections (see Sec. IV D, where this technique is explained in more detail). A typical example of the variation of the false neighbors number N_f with dimension of the embedding space N is presented in Fig. 14. The embedding dimension provides the size of the vector $\mathbf{x}_{D_e}(t) = [s(t), s(t - \Delta t^*), \dots, s(t - (D_e - 1)\Delta t^*)]$ that represents the state of the system at any given time t . Once D_e is known, a more precise estimate of the attractor dimension accounting

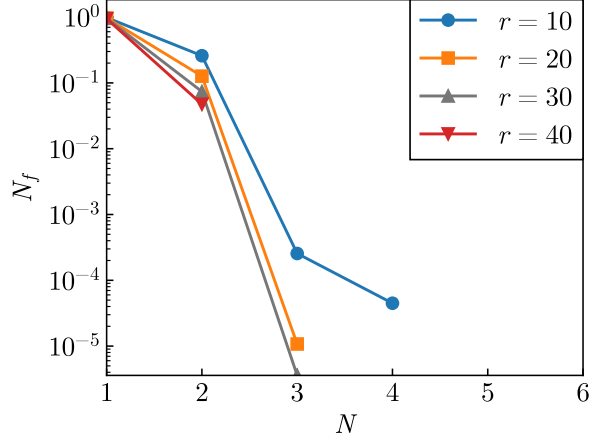


FIG. 14. Evolution of the number of false neighbors N_f for increasing phase-space dimension N for an acoustic forcing $A = 2.2$. Different critical divergence ratios r are tested and lead to different values for the embedding dimension D_e .

for the intricacies of the system dynamics is obtained by means of the correlation dimension D_2 [43]. D_2 is derived from the power law exponent of the correlation sum

$$C_2(D_e, \epsilon) = \frac{1}{N_{\text{pair}}} \sum_{i=D_e}^N \sum_{j=D_e}^{i-w} \Theta(\epsilon - \|\mathbf{x}_{D_e}(t_i) - \mathbf{x}_{D_e}(t_j)\|), \quad (12)$$

where ϵ is a threshold distance, $N_{\text{pair}} = (N - D_e - w)(N - D_e - w + 1)/2$ is the number of considered pairs of points, Θ is the Heaviside step function, t_i is the i th measurement instant, and w is a Theiler window to avoid considering consecutive points of a time series that are not independent [44]. The Theiler window is determined using the first minima of the space-time separation plot, as recommended by Kantz and Schreiber [40], and corresponds to times in the range $t = 4 \times 10^{-3}$ to 1.5×10^{-2} .

An example of the correlation sum is plotted in Fig. 15 for $A = 2.3$ and reveals a fractal correlation dimension of $D_2 = 2.35$. The variations of both the embedding and correlation dimensions (D_e and D_2) with A are represented in Fig. 16. Their variations are consistent with the evolution of the system identified in Sec. IV A: Both dimensions increase monotonously over the interval $1.5 \leq A \leq 2.3$ and suddenly drop for $A = 2.4$, when the dynamics brutally simplifies. D_e and D_2 start increasing again from $A = 2.4$ to $A = 3$. The second drop in dimension between $A = 3.1$ and $A = 3.13$ can be explained by the frequency-locking phenomenon discussed in Sec. III B. For $A \geq 3.15$, the dimension of the attractor increases significantly beyond the capabilities of the techniques we apply ($D_e > 10$).

The attractor for $A = 2.3$ stands out as it combines a quasiperiodic behavior and intermittent events. This can be identified in the topology of the attractor shown in Fig. 13, where a well-defined structure representing the quasiperiodic behavior (separately presented in a dotted square) is surrounded by vast clouds of points seeded by intermittent events (see the Supplemental Material illustrating this behavior [41]). Unfortunately, our total signal comprises only 25 such intermittent events and provides insufficient statistics to be able to extract the dimensions of the entire attractor. A precise estimate would require prohibitively long numerical simulations. Nevertheless, the attractor region corresponding to the quasiperiodic behavior is well populated and both the embedding and correlation dimensions of this region alone can be extracted by means of the methods described above. The correlation dimension of $D_2 = 2.35$ is characteristic of a fractal attractor, which indicates its chaotic nature.

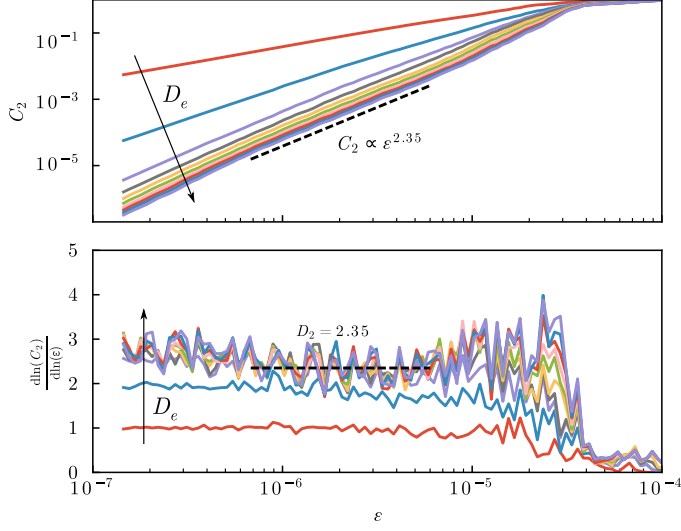


FIG. 15. Correlation sum C_2 computed from u'_t for an acoustic forcing $A = 2.3$. The correlation sum is computed for different embedding dimensions D_e in the range from $D_e = 1$ to 10 (represented by different colours) to ensure that it is not computed on a folded attractor. A fairly constant slope is observed in the scaling (central) range and indicates a fractal dimension of $D_2 = 2.35$. For small scales ($\epsilon < 7 \times 10^{-7}$), the correlation sum is known to be dominated by noise [40]. For large scales ($\epsilon > 5 \times 10^{-6}$), the self-similarity is broken by the finite extension of the attractor.

C. Maximal Lyapunov exponent

The chaotic behavior at $A = 2.3$ can be characterized further by computing the maximal Lyapunov exponent λ . λ is computed as the rate of spatial divergence in the phase space of two trajectories that are initially in the same neighborhood [45]. We find $\lambda = 7.69 > 0$, which, again, confirms the chaotic behavior of the dynamical system. The corresponding characteristic time ($T_\lambda = 1/\lambda = 0.13$) is of the same order of magnitude as the characteristic frequencies found in the spectral analysis in Sec. III ($T_a = 1/f_a = 0.15$). Visual inspection of the time evolution of pairs of neighboring points in the phase space for $A = 2.3$ (see Supplemental Material [41]) shows that the region of the attractor corresponding to intermittent events is a much greater source of chaos than the central part associated to a quasiperiodic behavior. Indeed, two initially close points remain

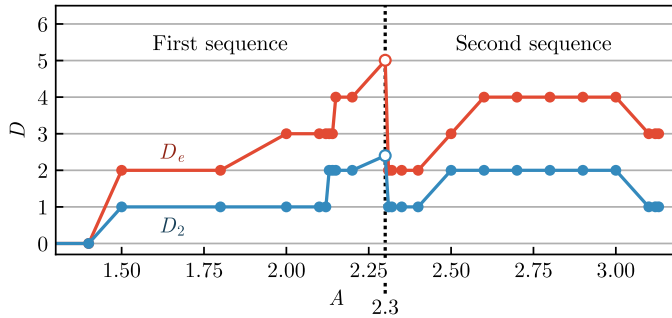


FIG. 16. Variations of the embedding and correlation dimensions (D_e and D_2) with the acoustic forcing A . The first and second sequences are clearly visible as consecutive increases of the dimensions separated by a sudden drop.

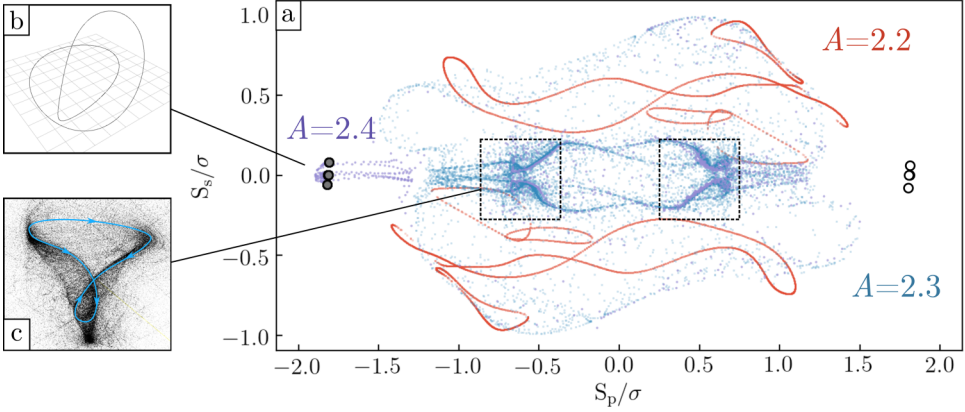


FIG. 17. (a) Comparison of the Poincaré section of the attractors for $A = 2.2$, $A = 2.3$, and $A = 2.4$. S_s and S_p are the coordinates of the intersections between the Poincaré section and the attractors. The signal is normalized using σ , the standard deviation of the time series for $A = 2.2$. The Poincaré section plane is obtained using POD to ensure an optimal perpendicularity with the attractor trajectories. For $A = 2.3$, this representation singles out the two unstable orbits (surrounded by dashed boxes), where the system remains 80% of the time. One of these orbits is represented in panel (c), in the three-dimensional phase space. The less dense outer region for $A = 2.3$ matches the region occupied by the attractor at $A = 2.2$. For $A = 2.4$, the attractor is represented with its transient part (purple points) that travels on the same Poincaré section as for $A = 2.3$, before stabilizing (four purple circles, with two of them being juxtaposed). The final attractor for $A = 2.4$ is represented in the three-dimensional phase space in panel (b). By symmetry, another attractor is supposed to exist for $A = 2.4$, as indicated by white circles.

close when in the central, dense region of the phase space but separate very quickly when one of them undergoes an intermittent event and wanders into the outer region.

In conclusion, the nonlinear analysis confirms the presence of chaos for $A = 2.3$. The fact that we were not able to compute nonlinear properties for $A > 3.13$ suggests that the increase in dimensions is very abrupt at the end of the second sequence. As a last step, we shall now analyze the particular case of $A = 2.3$ in more detail.

D. Poincaré sections and symmetry breaking

The case $A = 2.3$ deserves closer attention as it involves both quasiperiodic dynamics and intermittent behavior. To extract more information from the topology of the corresponding attractor, we shall represent its trace in Poincaré sections and compare it to that obtained for slightly lower and slightly higher forcing parameters ($A = 2.2$ and $A = 2.4$). They are presented in Fig. 17. To emphasize the symmetry breaking, we will use the time series of the vertical velocity fluctuation u'_z in the first jet at point S_1 [see Figs. 3(g) and 3(h)], rather than the time series of u'_t used thus far. The principal attractor directions are computed by proper orthogonal decomposition (POD); see Ref. [46], for example) to ensure that the Poincaré sections are plotted in planes of the phase space that are as close to perpendicular as possible to the attractor trajectories.

For $A = 2.2$, the Poincaré section is the trace of a T^2 torus, with the shape of a Klein bottle. This is consistent with the embedding dimension $D_e = 4$ and the correlation dimension $D_2 = 2$ found in the previous section. For $A = 2.3$, the Poincaré section exhibits two different regions that are the traces of the two regions we previously identified: (i) the outer region corresponds to intermittent events. The topology of this region matches that of the Poincaré section for $A = 2.2$. (ii) Two dense regions [in dotted boxes in Fig. 17(a)] contain approximately 80% of the points of the attractor. Their shape is close to a simple closed line [Fig. 17(c)]. The system jumps periodically from one dense set of orbits to the other. However, some of these jumps involve a long excursion into the outer parts of

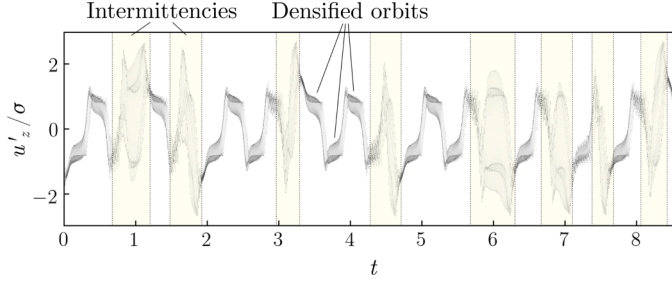


FIG. 18. Time evolution of u'_z for an acoustic forcing $A = 2.3$, normalized using the standard deviation of the time series σ . Vertical dotted lines delimit the regions of intermittencies.

the attractor which corresponds to an intermittent event. Figure 18 presents the time series of u'_z for $A = 2.3$, highlighting the successive switches between the densified orbits and the intermittencies. For $A = 2.4$, the system is periodic [Fig. 17(b)], which is indicated by four intersections with the Poincaré plane. However, the transient part of the signal obtained for $A = 2.4$ shows that the system travels for some time in the regions occupied by the attractor for $A = 2.3$, before converging to a periodic attractor.

Regarding the topology of the attractors, the evolution toward a chaotic behavior and the subsequent simplification of the dynamics follow the following scenario: the attractor consists of a well-defined T^2 torus for $A = 2.2$. It loses its stability for $A = 2.3$, where the dynamical system switches between three sets of unstable orbits. The two first sets consist of dense orbits that are quasiperiodic and symmetric to each other [as shown in Figs. 17(a), 17(c) and 18], while the third set is an orbit traveling through symmetric regions of the phase space that coincide with the attractor for $A = 2.2$. The system switches intermittently between the two sets of dense orbits by passing through the third one. This behavior is reminiscent of the Lorentz attractor, which exhibits two unstable orbits, with intermittent shifts from one to the other. For $A = 2.4$, the transient part of the signal (in purple in Fig. 17) shows that the system travels between the three previous sets of orbits, but finally ends up reaching a different basin of attraction, which corresponds to a state where the symmetry of the time-averaged velocity field with respect to the horizontal plane at $z = 0$ is broken.

It is noteworthy that due to the up-down symmetry of the geometry and of the forcing, another periodical attractor with opposite values of S_p/σ and S_s/σ [represented by white points in Fig. 17(a)] is expected to exist for $A = 2.4$. Moreover, the basin of attraction leading to the attractor presented for $A = 2.4$ could also be present for $A = 2.3$. In practice, however, it remains unexplored for $A = 2.3$ despite the wide excursions in the phase space. Surprisingly, the dense orbits of the configuration at $A = 2.3$ share the same characteristic frequency as the attractor for $A = 2.4$. This is somewhat unexpected as both represent different areas of the phase space which coexist (as shown by the transient part of the configuration at $A = 2.4$).

To conclude this part, the chaotic behavior of the system for $A = 2.3$ is linked to the appearance of two symmetric unstable orbits. It can be seen as an intermediate state that combines the dynamics of two nonchaotic states respectively found at slightly lower and slightly higher forcing parameters. This is also the last calculated state (in the sense of increasing A) before the symmetry of the time-averaged velocity field is broken.

E. High-dimensional systems

The nonlinear dynamics properties for acoustic forcing greater than $A = 3.2$ are challenging to obtain using the method described in the previous sections because of their high dimension (see Fig. 13). In such a case, relying on global quantities instead of local ones, as well as filtering the high frequencies, has been shown to help describe the dynamics [47,48]. Having investigated several global quantities in this spirit, the integral of the vertical vorticity in quarters of horizontal planes at

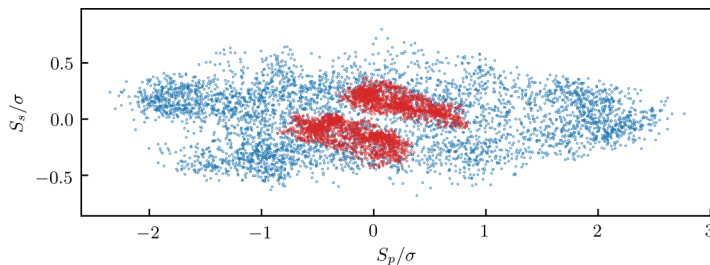


FIG. 19. Poincaré sections for a high-dimensional system ($A = 3.2$). The blue section is obtained from a local quantity (transverse velocity at the jet). The red section is obtained from a global quantity (integral of the vertical vorticity in one quarter of the horizontal plane at midheight of the lower half of the cavity). For both signals, high frequencies have been filtered out at $f = 1000$ using a Gaussian filter. A structure close to a 2D torus is clearly visible on the red section.

midheight of the upper half or lower half of the cavity came out as most useful. Analysis based on these quantities recovered the results obtained with local time series for low-dimensional systems (up to $A = 3.1$), in terms of embedding and correlation dimensions. For high-dimensional systems, global quantities whose high frequencies have been filtered out ($f > 1000$) using a phase-preserving Gaussian filter highlighted the presence of a 2D torus for an acoustic forcing of $A = 3.2$ (Fig. 19). This indicates that the 2D torus observed for $2.5 < A < 3.0$ persists at higher forcing but is concealed within the higher dimensional part of the attractor incurred by broad-band fluctuations likely associated to turbulence. For higher acoustic forcing such as $A = 4$, on the other hand, the intensity of the fluctuations becomes higher and time-series analysis of the global quantities does not reveal any recognisable structure.

V. CONCLUSION

We conducted frequency and dynamical systems analyses of the acoustically driven recirculating flow obtained through successive reflections of an acoustic beam on the walls of a square cavity. Both methods concur to show that the system can sustain states of low-dimensional chaos for specific values of the forcing parameter A that measures the intensity of the acoustic forcing. When increasing A , however, the systems follows a peculiar pathway to the chaotic state with a number of remarkable features: First, the transition to chaos splits into two consecutive phases, where a succession of Hopf and period-doubling bifurcations between oscillatory states of increasing complexity leads to potentially chaotic states. Between the end of the first phase and the beginning of the second ($2.3 < A < 2.4$), the dynamics of the system drastically simplifies. This rather unexpected behavior is consistent with previous experimental observations by Cambonie *et al.* [26], as are the low oscillation frequencies in the basic periodic states. During this complex evolution, the physical states of the system depart relatively little from the basic flow topology of the steady recirculating flow, with one notable exception: In the hinge state that immediately precedes the simplification of the dynamics, the time-averaged flow loses its up-down symmetry and fluctuations in the velocity field drop in intensity. Second, reconstruction of the underlying attractors out of the time series of the velocity field showed that the hinge state was indeed chaotic (with a positive Lyapounov exponent $\lambda = 7.69$ and a fractal correlation dimension of $D_2 = 2.35$). The topology of the attractor suggests that intermittencies arise from excursions of orbits between two distinct regions of the attractor. Each of these regions corresponds to the dynamics of the nonchaotic states respectively observed at slightly lower and slightly higher values of the forcing parameter ($A = 2.2$ and $A = 2.4$). Finally, the second phase of the evolution ends up in a seemingly high-dimensional state, where the structure of the 2D torus persists, but is concealed by the appearance of high-frequency, high-dimensional fluctuations. Along the way, a second simplification of the dynamics

arises out of a frequency-locking phenomenon at $A = 3.1$. The analysis of the regimes at high forcing ($A > 4$) remains an open challenge. The nature of the turbulence that may ensue may differ from that arising from the destabilisation of a classical free jet. This could significantly impact the mixing properties of the flow. The rich dynamics revealed in the present study raises the question of the existence of a dynamical model that would reproduce its succession of bifurcations. Such a model would notably allow for further study of the state of the system around the symmetry breaking and high acoustic forcing.

ACKNOWLEDGMENTS

The authors acknowledge support from the Carnot Institute Ingénierie@Lyon and the PHC Maghreb Partnership Program No. 36951NG. Support from the PMCS2I of Ecole Centrale de Lyon and the P2CHPD of University Lyon 1 for the numerical calculations is also gratefully acknowledged. The authors wish to thank Florence Raynal for fruitful discussions and Amine Kass for his work as a master student. Alban Pothérat is supported by a Royal Society Wolfson Research Merit Award (Ref. No. WM140032) and would like to express his gratitude to INSA-Lyon for the invited professor stays that made this collaboration possible.

-
- [1] M. Faraday, On a peculiar class of acoustical figures; and on certain forms assumed by groups of particles upon vibrating elastic surfaces, *Philos. Trans. R. Soc. London* **121**, 299 (1831).
 - [2] W. L. Nyborg, Acoustic streaming due to attenuated plane waves, *J. Acoust. Soc. Am.* **25**, 68 (2014).
 - [3] J. Lighthill, Acoustic streaming, *J. Sound Vib.* **61**, 391 (1978).
 - [4] N. Riley, Steady streaming, *Annu. Rev. Fluid Mech.* **33**, 43 (2001).
 - [5] B. Moudjed, V. Botton, D. Henry, H. Ben Hadid, and J.-P. Garandet, Scaling and dimensional analysis of acoustic streaming jets, *Phys. Fluids* **26**, 093602 (2014).
 - [6] B. Moudjed, V. Botton, D. Henry, S. Millet, J. P. Garandet, and H. Ben Hadid, Near-field acoustic streaming jet, *Phys. Rev. E* **91**, 033011 (2015).
 - [7] B. Moudjed, V. Botton, D. Henry, S. Millet, and H. Ben Hadid, Y-shaped jets driven by an ultrasonic beam reflecting on a wall, *Ultrasonics* **68**, 33 (2016).
 - [8] W. Dridi, D. Henry, and H. Ben Hadid, Influence of acoustic streaming on the stability of melt flows in horizontal Bridgman configurations, *J. Cryst. Growth* **310**, 1546 (2008).
 - [9] H. Ben Hadid, W. Dridi, V. Botton, B. Moudjed, and D. Henry, Instabilities in the Rayleigh-Bénard-Eckart problem, *Phys. Rev. E* **86**, 016312 (2012).
 - [10] A. Green, J. S. Marshall, D. Ma, and J. Wu, Acoustic streaming and thermal instability of flow generated by ultrasound in a cylindrical container, *Phys. Fluids* **28**, 104105 (2016).
 - [11] T. P. Lyubimova and R. V. Skuridin, Acoustic wave effect on a stability of convective flow in a horizontal channel subjected to the horizontal temperature gradient, *Int. J. Heat Mass Transf.* **104**, 478 (2017).
 - [12] B. Moudjed, V. Botton, D. Henry, S. Millet, J.-P. Garandet, and H. Ben Hadid, Oscillating acoustic streaming jet, *Appl. Phys. Lett.* **105**, 184102 (2014).
 - [13] H. Sato, The stability and transition of a two-dimensional jet, *J. Fluid Mech.* **7**, 53 (1960).
 - [14] P. S. Landa and P. V. E. McClintock, Development of turbulence in subsonic submerged jets, *Phys. Rep.* **397**, 1 (2004).
 - [15] L. Gorbunov, A. Pedchenko, A. Feodorov, E. Tomzig, J. Virbulis, and W. V. Ammon, Physical modelling of the melt flow during large-diameter silicon single crystal growth, *J. Cryst. Growth* **257**, 7 (2003).
 - [16] N. Bertin, R. Wunenburger, E. Brasselet, and J.-P. Delville, Liquid-Column Sustainment Driven by Acoustic Wave Guiding, *Phys. Rev. Lett.* **105**, 164501 (2010).
 - [17] D. G. Eskin, Ultrasonic Melt Processing: Achievements and Challenges, *Materials Science Forum* **828**, 112 (2015).

- [18] Y. K. Oh, S. H. Park, and Y. I. Cho, A study of the effect of ultrasonic vibrations on phase-change heat transfer, *Int. J. Heat Mass Transf.* **45**, 4631 (2002).
- [19] G. N. Kozhemyakin, Imaging of convection in a Czochralski crucible under ultrasound waves, *J. Cryst. Growth* **257**, 237 (2003).
- [20] G. N. Kozhemyakin, L. V. Nemets, and A. A. Bulankina, Simulation of ultrasound influence on melt convection for the growth of $\text{Ga}_x\text{In}_{1-x}\text{Sb}$ and Si single crystals by the Czochralski method, *Ultrasonics* **54**, 2165 (2014).
- [21] M. Chatelain, V. Botton, M. Albaric, D. Pelletier, B. Cariteau, D. Abdo, and M. Borrelli, Mechanical stirring influence on solute segregation during plane front directional solidification, *Int. J. Thermal Sci.* **126**, 252 (2018).
- [22] O. Bulliard-Sauret, S. Ferrouillat, L. Vignal, A. Memponteil, and N. Gondrexon, Heat transfer enhancement using 2 MHz ultrasound, *Ultrason. Sonochem.* **39**, 262 (2017).
- [23] J. S. Marshall and J. Wu, Acoustic streaming, fluid mixing, and particle transport by a Gaussian ultrasound beam in a cylindrical container, *Phys. Fluids* **27**, 103601 (2015).
- [24] C. Suri, K. Takenaka, H. Yanagida, Y. Kojima, and K. Koyama, Chaotic mixing generated by acoustic streaming, *Ultrasonics* **40**, 393 (2002).
- [25] M. C. Schenker, M. J. B. M. Pourquié, D. G. Eskin, and B. J. Boersma, PIV quantification of the flow induced by an ultrasonic horn and numerical modeling of the flow and related processing times, *Ultrason. Sonochem.* **20**, 502 (2013).
- [26] T. Cambonie, B. Moudjed, V. Botton, D. Henry, and H. Ben Hadid, From flying wheel to square flow: Dynamics of a flow driven by acoustic forcing, *Phys. Rev. Fluids* **2**, 123901 (2017).
- [27] J. L. McCauley, *Chaos, Dynamics, and Fractals: An Algorithmic Approach to Deterministic Chaos* (Cambridge University Press, Cambridge, UK, 1994).
- [28] D. Molenaar, H. J. H. Clercx, and G. J. F. van Heijst, Transition to Chaos in a Confined Two-Dimensional Fluid Flow, *Phys. Rev. Lett.* **95**, 104503 (2005).
- [29] H. D. I. Abarbanel, R. Brown, J. J. Sidorowich, and L. S. Tsimring, The analysis of observed chaotic data in physical systems, *Rev. Mod. Phys.* **65**, 1331 (1993).
- [30] D. T. Blackstock, *Fundamentals of Physical Acoustics*, 1st ed. (Wiley-Interscience, New York, 2000).
- [31] H. Ben Hadid and D. Henry, Numerical study of convection in the horizontal Bridgman configuration under the action of a constant magnetic field. Part 2. Three-dimensional flow, *J. Fluid Mech.* **333**, 57 (1997).
- [32] G. E. Karniadakis, M. Israeli, and S. A. Orszag, High-order splitting methods for the incompressible Navier-Stokes equations, *J. Comput. Phys.* **97**, 414 (1991).
- [33] S. Newhouse, D. Ruelle, and F. Takens, Occurrence of strange Axiom A attractors near quasiperiodic flows on T^m , $m \geq 3$, *Commun. Math. Phys.* **64**, 35 (1978).
- [34] J.-P. Eckmann, Roads to turbulence in dissipative dynamical systems, *Rev. Modern Phys.* **53**, 643 (1981).
- [35] M. J. Feigenbaum, Quantitative universality for a class of nonlinear transformations, *J. Stat. Phys.* **19**, 25 (1978).
- [36] M. J. Feigenbaum, The onset spectrum of turbulence, *Phys. Lett. A* **74**, 375 (1979).
- [37] M. J. Feigenbaum, The transition to aperiodic behavior in turbulent systems, *Commun. Math. Phys.* **77**, 65 (1980).
- [38] Y. Pomeau and P. Manneville, Intermittent transition to turbulence in dissipative dynamical systems, *Commun. Math. Phys.* **74**, 189 (1980).
- [39] P. D. Welch, The use of fast Fourier transform for the estimation of power spectra: A method based on time averaging over short, modified periodograms, *IEEE Trans. Audio Electroacoustics* **15**, 70 (1967).
- [40] H. Kantz and T. Schreiber, *Nonlinear Time Series Analysis*, 2nd ed. (Cambridge University Press, Cambridge, UK, 2004).
- [41] See Supplemental Material at <http://link.aps.org/supplemental/10.1103/PhysRevFluids.4.044401> for movies of the formation of chaotic and non-chaotic attractors in the three dimensional phase space.
- [42] M. B. Kennel, R. Brown, and H. D. I. Abarbanel, Determining embedding dimension for phase-space reconstruction using a geometrical construction, *Phys. Rev. A* **45**, 3403 (1992).

- [43] P. Grassberger and I. Procaccia, Measuring the strangeness of strange attractors, [Phys. D \(Amsterdam, Neth.\)](#) **9**, 189 (1983).
- [44] R. Hegger, H. Kantz, and T. Schreiber, Practical implementation of nonlinear time series methods: The TISEAN package, [Chaos](#) **9**, 413 (1999).
- [45] M. T. Rosenstein, J. J. Collins, and C. J. De Luca, A practical method for calculating largest Lyapunov exponents from small data sets, [Phys. D \(Amsterdam, Neth.\)](#) **65**, 117 (1993).
- [46] I. T. Jolliffe, *Principal Component Analysis* (Springer Science & Business Media, New York, 2002).
- [47] T. Buzug and G. Pfister, Optimal delay time and embedding dimension for delay-time coordinates by analysis of the global static and local dynamical behavior of strange attractors, [Phys. Rev. A](#) **45**, 7073 (1992).
- [48] D. Faranda, Y. Sato, B. Saint-Michel, C. Wiertel, V. Padilla, B. Dubrulle, and F. Daviaud, Stochastic Chaos in a Turbulent Swirling Flow, [Phys. Rev. Lett.](#) **119**, 014502 (2017).